

## Article

# Spinel-Structured, Multi-Component Transition Metal Oxide (Ni,Co,Mn)Fe<sub>2</sub>O<sub>4-x</sub> as Long-Life Lithium-Ion Battery Anode Material

Lishan Dong<sup>1,2,†</sup>, Zigang Wang<sup>1,†</sup>, Yongyan Li<sup>1,\*</sup>, Chao Jin<sup>1</sup>, Fangbing Dong<sup>1</sup>, Weimin Zhao<sup>1,\*</sup>, Chunling Qin<sup>1</sup>  and Zhifeng Wang<sup>1,2,\*</sup> 

<sup>1</sup> School of Materials Science and Engineering, Hebei University of Technology, Tianjin 300401, China

<sup>2</sup> Key Laboratory for New Type of Functional Materials in Hebei Province, Hebei University of Technology, Tianjin 300401, China

\* Correspondence: liyongyan@hebut.edu.cn (Y.L.); wmzhao@hebut.edu.cn (W.Z.);

wangzfb@hebut.edu.cn (Z.W.); Tel.: +86-22-60438000 (Y.L.); +86-22-60204477 (W.Z.); +86-22-60202006 (Z.W.)

† These authors contributed equally to this work.

**Abstract:** Metal oxide anode materials are affected by severe volume expansion and cracking in the charging/discharging process, resulting in low capacity and poor cycle stability, which limits their application in lithium-ion batteries (LIBs). Herein, a new strategy is uncovered for a preparing spinel-structured, multi-component transition metal oxide, (Ni,Co,Mn)Fe<sub>2</sub>O<sub>4-x</sub>, with oxygen vacancies as an LIB anode material. The as-fabricated material presented excellent reversible capacity and cycling stability, delivering a discharge capacity of 1240.2 mAh g<sup>-1</sup> at 100 mA g<sup>-1</sup> for 200 cycles and then at 300 mA g<sup>-1</sup> for 300 additional cycles. It presented extremely long cycle stability even at 2 A g<sup>-1</sup>, revealing 650.5 mAh g<sup>-1</sup> after 1200 cycles. The good lithium storage capacity can be ascribed to the entropy stabilization effect, the multi-cation synergistic effect, abundant oxygen vacancies and the spinel structure. This study provides a new opportunity to fabricate and optimize conversion-type anodes for LIBs with satisfactory electrochemical performance.

**Keywords:** dealloying; spinel; transition metal oxide; Li-ion battery; anode



**Citation:** Dong, L.; Wang, Z.; Li, Y.; Jin, C.; Dong, F.; Zhao, W.; Qin, C.; Wang, Z. Spinel-Structured, Multi-Component Transition Metal Oxide (Ni,Co,Mn)Fe<sub>2</sub>O<sub>4-x</sub> as Long-Life Lithium-Ion Battery Anode Material. *Batteries* **2023**, *9*, 54. <https://doi.org/10.3390/batteries9010054>

Academic Editors:  
Simon Wiemers-Meyer and  
Richard Schmuck

Received: 15 December 2022  
Revised: 7 January 2023  
Accepted: 10 January 2023  
Published: 12 January 2023



**Copyright:** © 2023 by the authors. Licensee MDPI, Basel, Switzerland. This article is an open access article distributed under the terms and conditions of the Creative Commons Attribution (CC BY) license (<https://creativecommons.org/licenses/by/4.0/>).

## 1. Introduction

A great challenge for advanced batteries is the successive exploration of electrode materials with excellent energy density and stable performance to meet the ever-increasing demands in the field of smart grids and electric vehicles [1–3]. The ideal electrode should meet the demands of high Li storage capacity, low lithiation/delithiation potential and high ionic conductivity [4]. Transition metal oxides (TMOs) have been regarded as potential anode materials because of their high energy density, suitable potential and abundant resources since they were proposed in 2000 [5]. The mechanism for Li storage is associated with a conversion reaction that follows the equation of MO<sub>x</sub> + 2xLi ↔ M + xLi<sub>2</sub>O, where M refers to transition metals such as Co, Fe, Ni and Cu [6]. Accompanied by the conversion reactions that occur, the structure and morphology of active electrode particles completely change during the regeneration of the initial particles when charging a perfect conversion-type electrode [4,7,8]. Unfortunately, the voltage hysteresis caused by reaction limitations usually leads to lower energy efficiency and poor capacity. Moreover, TMOs can catalyze the decomposition of electrolytes to some extent and thus deteriorate the cycle life of batteries. The severe volume changes during the charging/discharging process usually induce the cracking and pulverization of active particles and further damage the performance [9–13].

To solve the problem of pulverization and improve cycling stability, it was reported that the introduction of additional atoms on the basis of a single transition metal oxide can be an effective approach [14–16]. The lithium storage performance of bimetallic

oxides such as  $AFe_2O_4$  ( $A = Zn, Ni, Co, Cu, Cd$ ) [15] and  $MCo_2O_4$  ( $M = Mn, Zn, Fe, Ni, Co$ ) [14,17,18] and high-entropy oxides (HEOs) such as  $(FeCoNiCrMn)_3O_4$  [19–22] and  $(CrMnFeNiCu)_3O_4$  [23,24] were reported, which confirmed that multi-component oxides can effectively inhibit the phenomenon of pulverization through stepwise lithium storage. Furthermore, the introduction of rationally designed nanostructures could also provide an efficient diffusion pathway for  $Li^+$ , thereby enhancing the reaction kinetics [25–28]. Therefore, it is necessary to make further efforts and adopt reasonable design strategies to develop TMO anode materials with good cycle stability and high specific capacity that are suitable for practical applications.

Inspired by the aforementioned progress, we open up a new opportunity for the fabrication of a multi-component TMO as anode for LIBs. A spinel-structured,  $AB_2O_4$ -type, multi-component transition metal oxide,  $(Ni,Co,Mn)Fe_2O_4$ , with oxygen vacancies was obtained by dealloying  $(Ni_{0.2}Co_{0.2}Mn_{0.2}Fe_{0.4})_5Al_{95}$ , where Ni, Co and Mn occupy the A sites and Fe occupies the B sites. The synergism of multiple metal cations resulted in a stable cycle life, which could be cycled for more than 1200 times at  $2 A g^{-1}$  with no dramatic performance fading. Meanwhile, a large number of oxygen vacancies were found to promote the adsorption toward the Li atom and boost the electrochemical reactivity according to density functional theory (DFT) calculations. Moreover, combined with SEM observations, the active material showed a stable structural retention capacity during the (de)lithiation process because of the entropy stabilization effect. The current study discloses a route for the fabrication of spinel-structured, multi-component transition metal oxides, which can have positive effects on the composition design and development of novel anode materials for LIB applications.

## 2. Materials and Methods

The materials were prepared using the previously reported melt-spinning and dealloying method [29–32]. Firstly, an electric-arc-melted  $NiCoMnFe_2$  high-entropy alloy ingot and an Al ingot were remelted to form a  $Ni_2Co_2Mn_2Fe_4Al_{90}$  master alloy ingot. After that,  $Ni_2Co_2Mn_2Fe_4Al_{90}$  ribbons (3 mm wide, 20  $\mu m$  thick and several centimeters long) were produced using the melt-spinning technique. Then, 2 g of as-obtained ribbons was etched in 1 M NaOH solutions (500 mL) at 25  $^{\circ}C$  for 12 h and cleaned thrice with ultrapure water. Finally, the product was placed in an oven and dried for 12 h at 70  $^{\circ}C$  for follow-up tests. In the etching process, Al atoms were corroded away from the precursor, while the residual Ni, Co, Mn and Fe atoms were self-assembled and oxidized to multi-element transition metal oxide  $(Ni,Co,Mn)Fe_2O_{4-x}$  nanoplates. A schematic of the material fabrication process is displayed in Figure 1. Two contrast materials of pure  $Fe_3O_4$  and  $Fe_3O_4/Mn_3O_4$  composite were also synthesized by etching  $Fe_{10}Al_{90}$  and  $Fe_5Mn_5Al_{90}$  ribbons, respectively, through the same process. Material characterization, electrochemical measurements and DFT calculation processes are introduced in detail in Supporting S1.

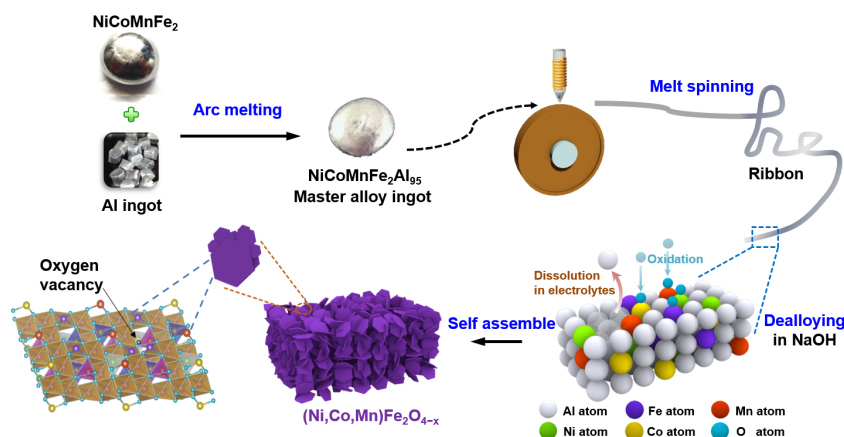
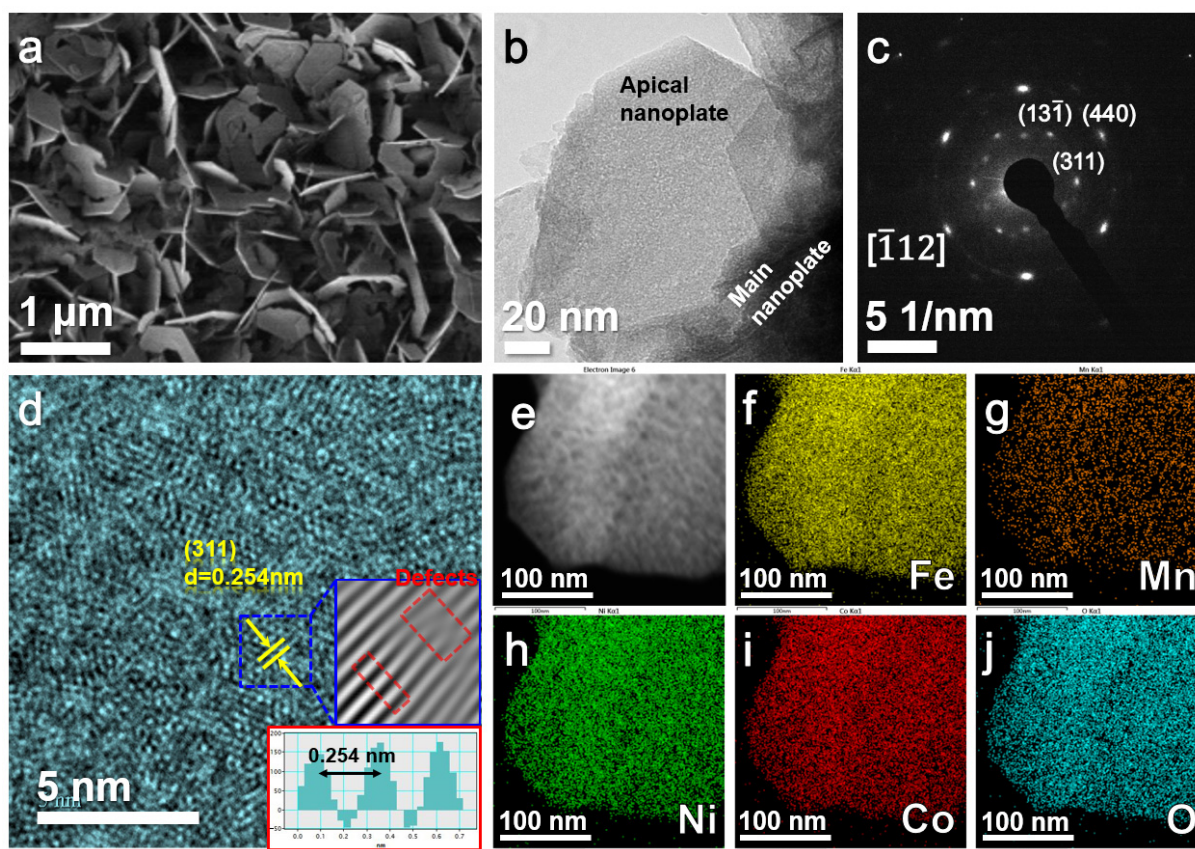


Figure 1. Schematic revealing the preparation process of  $(Ni,Co,Mn)Fe_2O_{4-x}$ .

### 3. Results and Discussion

The SEM images of the three dealloyed products are presented in Figure S1a–c. All the samples displayed nanoplate morphology. With the increase in the element types of the precursors, the size of the nanoplates decreased gradually. Figure S1d–g compare the length and thickness of the nanoplates in the three samples. The length of the nanoplates was reduced from several microns (dealloyed  $\text{Fe}_{10}\text{Al}_{90}$ ) to less than 1 micron (dealloyed  $\text{Ni}_2\text{Co}_2\text{Mn}_2\text{Fe}_4\text{Al}_{90}$ ), while the thickness of the nanoplates was reduced from hundreds of nanometers (dealloyed  $\text{Fe}_{10}\text{Al}_{90}$ ) to tens of nanometers (dealloyed  $\text{Ni}_2\text{Co}_2\text{Mn}_2\text{Fe}_4\text{Al}_{90}$ ). Figure 2 characterizes dealloyed  $\text{Ni}_2\text{Co}_2\text{Mn}_2\text{Fe}_4\text{Al}_{90}$  in more detail. Figure 2a,b reveal the special morphology of these nanoplates, showing that some small nanoplates (tens of nanometers in diameter) grew on the tip of the main nanoplates ( $\sim 1 \mu\text{m}$  in diameter). The corresponding SAED patterns (Figure 2c) consisted of diffraction spots, corresponding to the (311),  $(13\bar{1})$  and (440) planes of spinel structure oxides such as  $\text{NiFe}_2\text{O}_4$  with a zone axis of  $[\bar{1}12]$  [33]. The HRTEM image in Figure 2d shows that the interplanar distance was around 0.254 nm, relating to the (311) planes of the spinel structure oxide. In addition, there were a large number of defects formed by the vacancy of oxygen on material surfaces [34]. EPR tests (Figure S2) further uncovered the existence of oxygen vacancies [35], which can provide abundant active sites for electrochemical reactions in batteries. Figure 2e–j and Figure S3a show EDS elemental mappings of the as-prepared material, demonstrating a uniform distribution of O, Ni, Co, Mn and Fe elements. The atomic ratio of O:Fe:Co:Ni:Mn was approximately 56.18:29.51:4.84:5.01:4.46, as detected using EDS (Figure S3b). All the above results confirm that the dealloyed product was  $(\text{Ni},\text{Co},\text{Mn})\text{Fe}_2\text{O}_4$  with abundant oxygen vacancies, namely,  $(\text{Ni},\text{Co},\text{Mn})\text{Fe}_2\text{O}_{4-x}$ , in this work.



**Figure 2.** (a) SEM image, (b) TEM image, (c) SAED patterns, (d) HRTEM image and (e–j) EDS elemental mappings of as-prepared  $(\text{Ni},\text{Co},\text{Mn})\text{Fe}_2\text{O}_{4-x}$  material.

To study the crystal structure of NiCoMnFe<sub>2</sub>, the precursors and the corresponding dealloyed products, XRD tests were performed (Figure 3a and Figure S4). In Figure 3a, the NiCoMnFe<sub>2</sub> alloy exhibits an fcc structure with typical diffraction lattice planes of (111), (200), (220) and (311) [36]. After alloying with Al, it mainly presented Al phase, Fe phase and Al-M phases (M = Mn, Ni and Co), which was similar to the solidification phase of the Fe<sub>10</sub>Al<sub>90</sub> and Fe<sub>5</sub>Mn<sub>5</sub>Al<sub>90</sub> precursors (Figure S4a–c). After dealloying, however, the corresponding oxides could be obtained. Fe<sub>3</sub>O<sub>4</sub> and Fe<sub>3</sub>O<sub>4</sub>/Mn<sub>3</sub>O<sub>4</sub> could be identified from the dealloyed Fe<sub>10</sub>Al<sub>90</sub> and Fe<sub>5</sub>Mn<sub>5</sub>Al<sub>90</sub> products, respectively (Figure S4d,e), while spinel oxides with (311), (400) and (440) diffraction lattice planes [37] could be found for dealloyed Ni<sub>2</sub>Co<sub>2</sub>Mn<sub>2</sub>Fe<sub>4</sub>Al<sub>90</sub> (Figure 3a). The diffraction peaks of this spinel oxide were near those of NiFe<sub>2</sub>O<sub>4</sub>, CoFe<sub>2</sub>O<sub>4</sub> and MnFe<sub>2</sub>O<sub>4</sub> and could be attributed to (Ni,Co,Mn)Fe<sub>2</sub>O<sub>4-x</sub> according to the series of the above results. With the enhancement of the components, the peak intensity declined, and the peak width widened. These diffraction peaks of as-obtained polyoxides are similar to those of some high-entropy oxides [37–39].

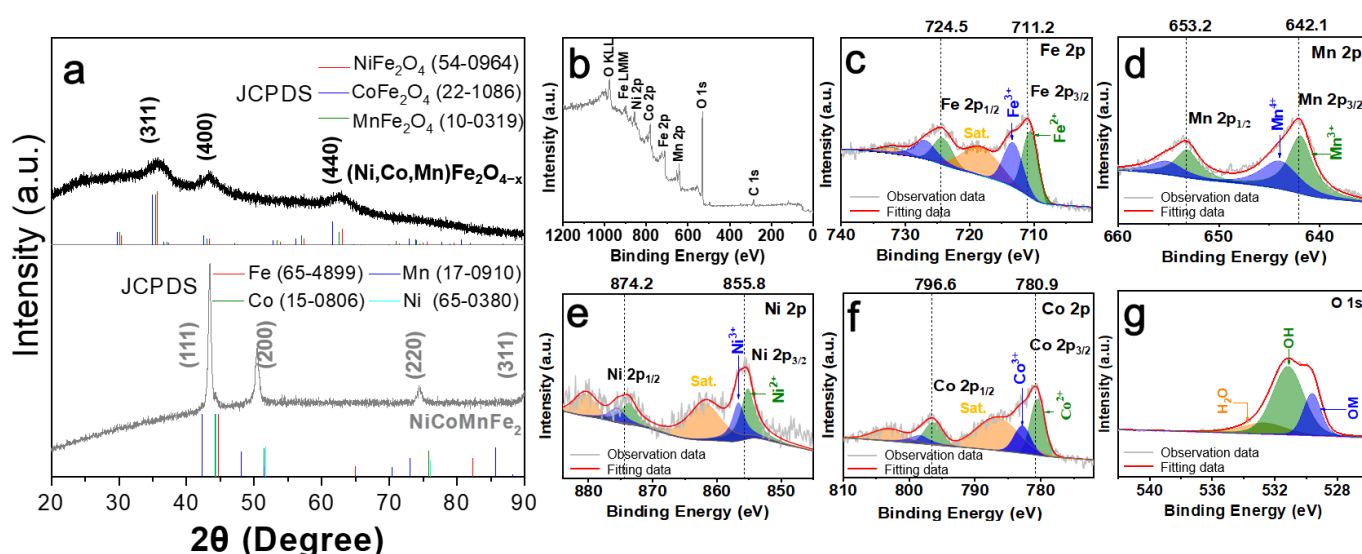


**Figure 3.** (a) XRD patterns of pristine NiCoMnFe<sub>2</sub> and dealloyed (Ni,Co,Mn)Fe<sub>2</sub>O<sub>4-x</sub> oxides. (b–g) XPS spectra of (Ni,Co,Mn)Fe<sub>2</sub>O<sub>4-x</sub>: (b) XPS survey spectra; (c–g) high-resolution core-level spectra of Fe 2p, Mn 2p, Ni 2p, Co 2p and O 1s, respectively.

An XPS test was performed to analyze the element and valence state of dealloyed Ni<sub>2</sub>Co<sub>2</sub>Mn<sub>2</sub>Fe<sub>4</sub>Al<sub>90</sub>. The XPS survey spectrum demonstrated the co-existence of Mn, Fe, Ni, Co and O elements (Figure 3b), which was in good agreement with the EDS result (Figure 2e–j). Figure 3c displays that the Fe 2p spectra of the dealloyed product were composed of two main peaks at 724.5 eV (Fe 2p<sub>1/2</sub>) and 711.2 eV (Fe 2p<sub>3/2</sub>) [40]. The Fe 2p<sub>1/2</sub> peak was superimposed by two doublets (724.4 eV and 727.1 eV), while Fe 2p<sub>3/2</sub> was composed by two doublets at 710.6 eV and 713.4 eV. The green peaks at 710.6 eV and 724.4 eV corresponded to Fe<sup>2+</sup>; meanwhile, the blue peaks at 713.4 eV and 727.1 eV were related to Fe<sup>3+</sup> [41–43]. The orange peaks represented satellite peaks of the corresponding main peaks. Similar doublets could also be found in the core-level spectra of Co 2p, Ni 2p and Mn 2p. Both the bivalent and trivalent (Ni, Co), as well as trivalent and tetravalent (Mn), states of these elements could be discovered [44–46]. The O 1s core-level spectrum (Figure 3g) was divided into three peaks [47]. The peak at 531.1 eV could be attributed to OH<sup>-</sup>, which probably originated from the residual etchant (NaOH). The peak located at 529.7 eV was due to the OM oxygen (M refers to metals), relating to the O<sup>2-</sup> in the metal oxide. The other peak at 533.2 eV related to O in H<sub>2</sub>O.

Figure 4 presents the N<sub>2</sub> adsorption–desorption isotherm and the matching pore-size distribution of the (Ni,Co,Mn)Fe<sub>2</sub>O<sub>4-x</sub> sample. A type III curve with an H3-type hysteresis loop is revealed in Figure 4a [29], demonstrating the existence of plentiful

mesopores on the nanoplates (Figure 2e). The specific surface area of the material was about  $112.69 \text{ m}^2 \text{ g}^{-1}$ , which was higher than those of spinel  $\text{CoFe}_2\text{O}_4$  and  $\text{NiFe}_2\text{O}_4$  oxide nanosheets ( $40\sim 90 \text{ m}^2 \text{ g}^{-1}$ ) obtained with traditional dealloying [47,48]. The pore size mainly ranged from 1.5 to 10 nm (Figure 4b). These micropores and mesopores increased the contact areas between the electrolyte and the active materials [49].

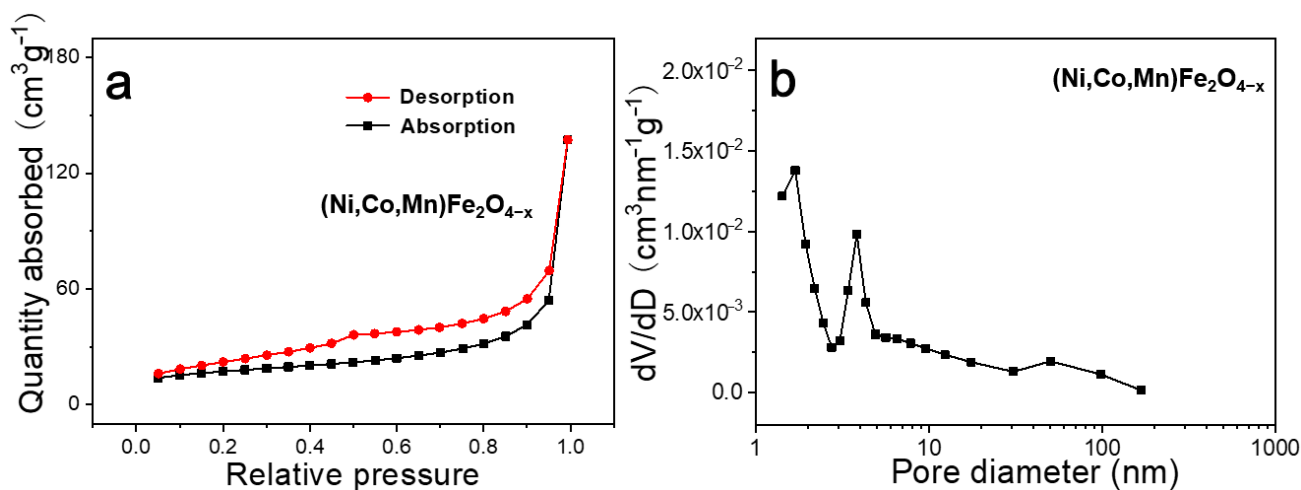


**Figure 4.**  $\text{N}_2$  adsorption–desorption isotherm of  $(\text{Ni,Co,Mn})\text{Fe}_2\text{O}_{4-x}$  (a) and corresponding pore-size distribution (b).

To reveal the electrochemical performance of the three dealloying products ( $(\text{Ni,Co,Mn})\text{Fe}_2\text{O}_{4-x}$ ,  $\text{Fe}_3\text{O}_4/\text{Mn}_3\text{O}_4$  and  $\text{Fe}_3\text{O}_4$ ), a series of tests were carried out (Figure 5). Cyclic voltammetry (CV) curves of the battery assembled with a  $(\text{Ni,Co,Mn})\text{Fe}_2\text{O}_{4-x}$  anode were measured, as shown in Figure 5a, at  $0.1 \text{ mV/s}$  within  $0.01\sim 3.0 \text{ V}$ . The CV curves of the three products (Figure 5a and Figure S5) are similar in shape (with a certain extent of position offset) but differ in peak intensities. It can be seen that the CV curves of  $\text{Fe}_3\text{O}_4$  and  $\text{Fe}_3\text{O}_4/\text{Mn}_3\text{O}_4$  show relatively sharp redox peaks, while that of  $(\text{Ni,Co,Mn})\text{Fe}_2\text{O}_{4-x}$  presents broad redox peaks, indicating that its reaction was not completed in a short time and in a rapid way but was carried out slowly in successive substeps. This electrochemical reaction characteristic displays a vital function in alleviating the huge volume variation during the cycle and inhibiting the cracking and pulverization of the active materials. In the initial cycle, two cathodic peaks at  $1.2 \text{ V}$  and  $0.6 \text{ V}$  can be found (Figure 5a), which corresponded to the reduction of metallic oxides to corresponding metal states and the creation of  $\text{Li}_2\text{O}$  [50]. In the following cycles, the reduction peaks shift to  $1.5 \text{ V}$  and  $0.8 \text{ V}$ . This position offset was the result of the formation of an SEI layer and the surface structural rearrangement of active materials in the lithiation process. The redox peaks nearly remain changeless after three cycles, reflecting the excellent cycling stability and reversibility of the  $(\text{Ni,Co,Mn})\text{Fe}_2\text{O}_{4-x}$  anode. The  $\text{Mn}_3\text{O}_4/\text{Fe}_3\text{O}_4$  electrode and the  $\text{Fe}_3\text{O}_4$  electrode show a CV tendency similar to that of the  $(\text{Ni,Co,Mn})\text{Fe}_2\text{O}_{4-x}$  anode in the first two cycles but much sharper recession in the closed area after three cycles (Figure S5), revealing their bad cycling stability. In the charging process, the  $\text{Fe}_3\text{O}_4$  electrode shows clear and sharp peaks at  $1.1 \text{ V}$ ,  $1.5 \text{ V}$  and  $1.8 \text{ V}$ , relating to two-step oxidation from  $\text{Fe}^0$  to  $\text{Li}_x\text{Fe}_3\text{O}_4$  and from  $\text{Li}_x\text{Fe}_3\text{O}_4$  to  $\text{Fe}^{3+}$ , respectively (Figure S5a). For the  $(\text{Ni,Co,Mn})\text{Fe}_2\text{O}_{4-x}$  electrode, however, two broad anodic peaks around  $1.5 \text{ V}$  and  $2.1 \text{ V}$  can be seen, corresponding to the intertwined multistep oxidation of multiple metals, Fe, Co, Mn and Ni, to their oxides. The CV curves of the  $(\text{Ni,Co,Mn})\text{Fe}_2\text{O}_{4-x}$  electrode present better repeatability than those of the  $\text{Mn}_3\text{O}_4/\text{Fe}_3\text{O}_4$  electrode and the  $\text{Fe}_3\text{O}_4$  electrode, implying its good cycling stability and reversibility.

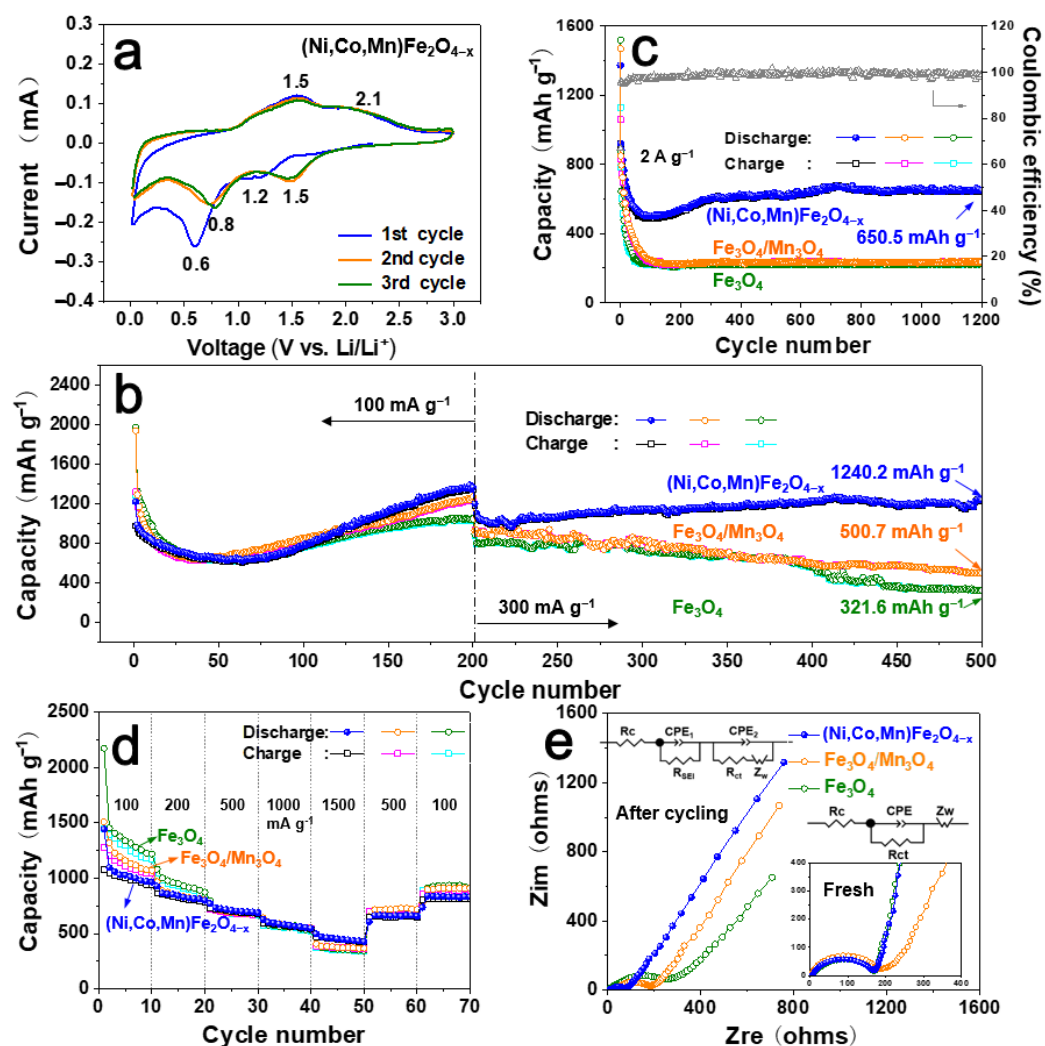


**Figure 5.** Electrochemical performance of the as-prepared  $(\text{Ni,Co,Mn})\text{Fe}_2\text{O}_{4-x}$ . (a) Cyclic voltammetry tested at 0.01–3 V at a scan rate of 0.1 mV/s. (b,c) Long cycle performance at different current densities: (b)  $100 \text{ mA g}^{-1}$  for 200 cycles and  $300 \text{ mA g}^{-1}$  for the following 300 cycles and (c)  $2 \text{ A g}^{-1}$  for 1200 cycles. (d) Rate performance at varied current densities ranging 100–1500  $\text{mA g}^{-1}$ . (e) Nyquist plots of fresh cells (inset) and cells after cycling.

Figure S6a shows the representative galvanostatic profiles of the  $(\text{Ni,Co,Mn})\text{Fe}_2\text{O}_{4-x}$  anode at  $100 \text{ mA g}^{-1}$  for different cycles. There are two discharge platforms at 1.4–1.7 V and 0.6–0.9 V, respectively, in the discharging process, while two charging platforms, 1.4–1.7 V and 2.0–2.5 V, can be found in the charging process. The above platform potential ranges correspond well with the peak voltage in the CV curve. The first charging/discharge capacity was about  $978.5/1223.1 \text{ mAh g}^{-1}$  with a first Coulombic efficiency of 80%. This serious capacity loss was probably induced by the generation of irreversible SEI films [51,52]. As the number of cycles increases (1–50 cycles), the charge/discharge curve gradually moves to the left, indicating that the battery capacity gradually decreased. On the other hand, as the number of cycles further increases, the battery capacity increased slowly. It can be seen that the reversible capacity at the 200th cycle was even higher than that at the first cycle. In the following cycles, the battery was tested at  $300 \text{ mA g}^{-1}$  (Figure S6b). The curves at the 201st, 300th, 400th and 500th cycles are close to each other, revealing that the  $(\text{Ni,Co,Mn})\text{Fe}_2\text{O}_{4-x}$  electrode possessed good electrochemical stability in later cycling.

Figure 5b shows the cycling performance of the three materials at  $100 \text{ mA g}^{-1}$  for 200 cycles and then at  $300 \text{ mA g}^{-1}$  for 300 cycles. During the first 66 cycles, the reversible capacity of  $(\text{Ni,Co,Mn})\text{Fe}_2\text{O}_{4-x}$  slowly reduced to about  $630 \text{ mAh g}^{-1}$  and then gradu-

ally increased to  $1369.9 \text{ mAh g}^{-1}$  (at the 200th cycle). This phenomenon is known as the U-shape increase [53,54], which is usually found in transition metal oxide materials. The decrease in the initial tens of cycles was due to the consumption of SEI film, the rearrangement of the atomic structure on the material surface and electrode activation, while the increase in the later period may have been related to the consumption of electrolyte. At the same time, the  $\text{Fe}_3\text{O}_4/\text{Mn}_3\text{O}_4$  and  $\text{Fe}_3\text{O}_4$  electrodes presented higher first discharge capacity than  $(\text{Ni,Co,Mn})\text{Fe}_2\text{O}_{4-x}$ , while their capacities dropped dramatically. The reversible capacities reached their lowest points after cycling for about 35 cycles. Although the capacities of both cells ( $\text{Fe}_3\text{O}_4/\text{Mn}_3\text{O}_4$  and  $\text{Fe}_3\text{O}_4$ ) gradually increased during subsequent cycles, the increase rate was relatively slower than that of  $(\text{Ni,Co,Mn})\text{Fe}_2\text{O}_{4-x}$ . At the 200th cycle, the reversible capacities reached  $1275.8$  ( $\text{Fe}_3\text{O}_4/\text{Mn}_3\text{O}_4$ ) and  $1051.3$  ( $\text{Fe}_3\text{O}_4$ ), which were lower than the  $1389.9$  of  $(\text{Ni,Co,Mn})\text{Fe}_2\text{O}_{4-x}$ . During the following 300 cycles at  $300 \text{ mA g}^{-1}$ , the  $(\text{Ni,Co,Mn})\text{Fe}_2\text{O}_{4-x}$  electrode showed good cycling stability. It maintained a discharge capacity of  $1240.2 \text{ mAh g}^{-1}$  after the latest 300 cycles, while those of the other anodes dropped dramatically, delivering the reversible capacities of  $500.7$  ( $\text{Fe}_3\text{O}_4/\text{Mn}_3\text{O}_4$ ) and  $321.6$  ( $\text{Fe}_3\text{O}_4$ )  $\text{mAh g}^{-1}$ , respectively. The above results demonstrate that the  $(\text{Ni,Co,Mn})\text{Fe}_2\text{O}_{4-x}$  electrode presented the best electrochemical property among the three anodes in long cycling.

Figure 5c shows the cyclic performance of the three electrodes cycling at a high current density of  $2 \text{ A g}^{-1}$  for 1200 cycles. During cycling, the capacities of  $\text{Fe}_3\text{O}_4/\text{Mn}_3\text{O}_4$  and  $\text{Fe}_3\text{O}_4$  electrodes decreased sharply and resulted to be around  $230 \text{ mAh g}^{-1}$  after 1200 cycles, while the U-shape increase could also be found for the  $(\text{Ni,Co,Mn})\text{Fe}_2\text{O}_{4-x}$  electrode. It delivered  $650.5 \text{ mAh g}^{-1}$  after 1200 cycles. Figure 5d shows the rate performance of the three electrodes at increased current densities from  $50$  to  $1500 \text{ mA g}^{-1}$ . Although the  $(\text{Ni,Co,Mn})\text{Fe}_2\text{O}_{4-x}$  electrode displayed relatively low reversible capacity when cycling at  $50 \text{ mA g}^{-1}$  (low current density), among the three electrodes, it presented the best reversible capacity when cycling at higher current densities ( $500\text{--}1500 \text{ mA g}^{-1}$ ). It delivered discharge capacities of  $1003$ ,  $891$ ,  $747$ ,  $661$  and  $508 \text{ mAh g}^{-1}$  at  $50$ ,  $100$ ,  $500$ ,  $1000$  and  $1500 \text{ mA g}^{-1}$ , respectively. The reversible capacity of the  $(\text{Ni,Co,Mn})\text{Fe}_2\text{O}_{4-x}$  electrode could be recovered as  $809 \text{ mAh g}^{-1}$  when cycling at  $100 \text{ mA g}^{-1}$  again, indicating acceptable reversibility. The voltage profiles of the three electrodes at the current density of  $1500 \text{ mA g}^{-1}$  are presented in Figure S6c, uncovering an obvious advantage in the charge/discharge capacity of  $(\text{Ni,Co,Mn})\text{Fe}_2\text{O}_{4-x}$  compared with those of  $\text{Fe}_3\text{O}_4/\text{Mn}_3\text{O}_4$  and  $\text{Fe}_3\text{O}_4$ . Figure 5e shows the EIS diagram of the three electrodes before and after cycling. The EIS curves show semicircles in the high-frequency area and oblique lines in the low-frequency region, relating to charge transfer resistance and ion diffusion resistance, respectively. Though the EIS diagram of the three fresh electrodes shows similar curve shapes and overlap among them to a certain extent, the  $(\text{Ni,Co,Mn})\text{Fe}_2\text{O}_{4-x}$  electrode showed the lowest resistance after cycling for 500 cycles, which can explain the good cycle stability of the battery in the long cycling process. Table S2 presents the Li-ion diffusion coefficients calculated using EIS; it can be seen that  $(\text{NiCoMn})\text{Fe}_2\text{O}_{4-x}$  showed a higher diffusion coefficient after cycling than the fresh one, revealing good reaction kinetics of  $(\text{NiCoMn})\text{Fe}_2\text{O}_{4-x}$ . On the other hand, the diffusion coefficients of the contrast materials were decreased, demonstrating their poor reaction kinetics.

In order to reveal the structural stability of the electrode materials during the cycling process, the SEM images of the  $(\text{Ni,Co,Mn})\text{Fe}_2\text{O}_{4-x}$ ,  $\text{Fe}_3\text{O}_4/\text{Mn}_3\text{O}_4$  and pure  $\text{Fe}_3\text{O}_4$  electrodes before and after cycling were characterized (Figure 6a–f). Figure 6a and b show that  $(\text{Ni,Co,Mn})\text{Fe}_2\text{O}_{4-x}$  retained its initial nanoplate shape without any crack or pulverization phenomenon, though it expanded its size slightly (from  $0.5\text{--}1 \mu\text{m}$  to  $2\text{--}3 \mu\text{m}$ ) after cycling. Different from the phenomenon of  $(\text{Ni,Co,Mn})\text{Fe}_2\text{O}_{4-x}$ , the contrast  $\text{Fe}_3\text{O}_4/\text{Mn}_3\text{O}_4$  (Figure 6c,d) and pure  $\text{Fe}_3\text{O}_4$  (Figure 6e,f) electrodes expanded and cracked significantly after cycling from  $1\text{--}2 \mu\text{m}$  to  $20\text{--}30 \mu\text{m}$  and from  $3\text{--}4 \mu\text{m}$  to  $50\text{--}80 \mu\text{m}$ , respectively. Figure 6g uncovers a schematic diagram of the structural changes in the three electrodes before and after cycling. It can be found that mono-metal oxide  $\text{Fe}_3\text{O}_4$  develops drastic expansion

and severe cracking after cycling. The expansion and cracking degree of  $\text{Fe}_3\text{O}_4/\text{Mn}_3\text{O}_4$  are alleviated with the increase in oxide components. However, the expansion and cracking of  $(\text{Ni},\text{Co},\text{Mn})\text{Fe}_2\text{O}_{4-x}$  are significantly inhibited when more elements are added. This phenomenon is related to the composition of the material, but also to the initial size of the material. Moreover, slight expansion and no crack correspond to relatively good cyclic stability, while severe expansion and cracking of the active material lead to the drastic deterioration of the electrochemical properties. The changes in these electrode materials are consistent with the current electrochemical properties.

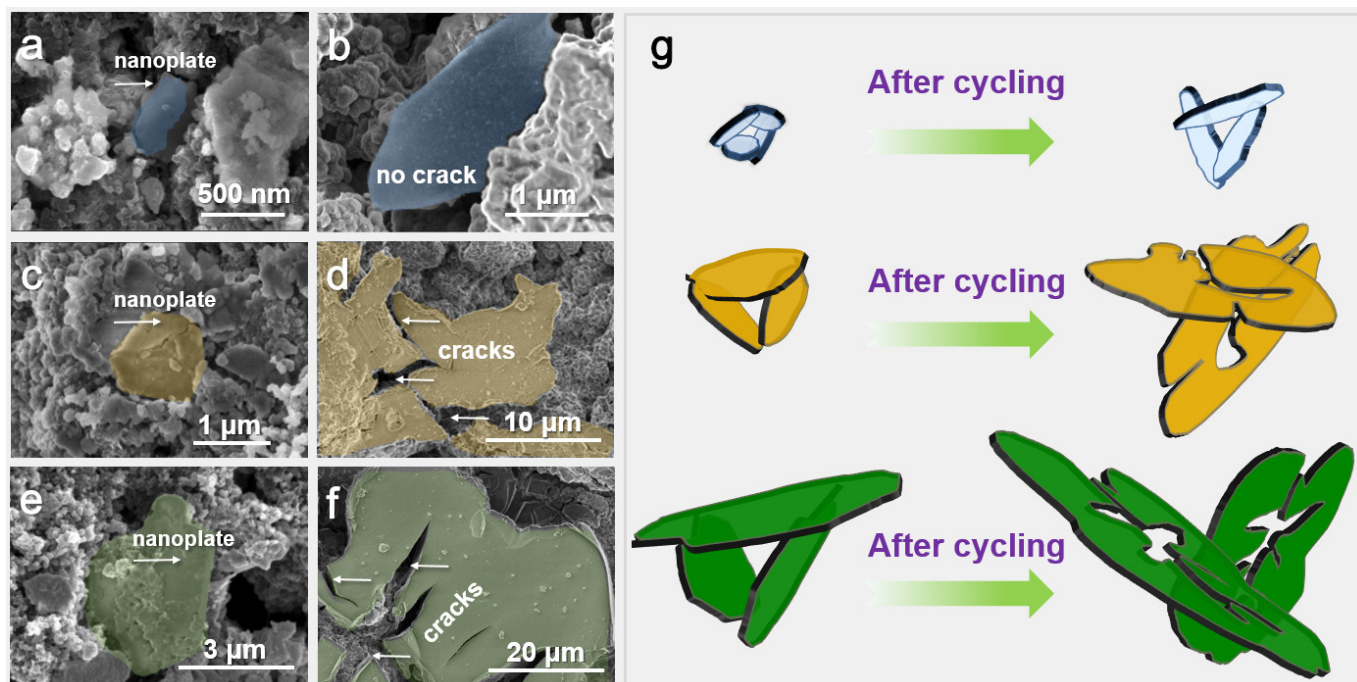


**Figure 6.** SEM images of (a,b)  $(\text{Ni},\text{Co},\text{Mn})\text{Fe}_2\text{O}_4$ , (c,d)  $\text{Fe}_3\text{O}_4/\text{Mn}_3\text{O}_4$  and (e,f)  $\text{Fe}_3\text{O}_4$  electrodes before (a,c,e) and after (b,d,f) cycling at  $100 \text{ mA g}^{-1}$  for 200 cycles. (g) Schematic diagram of the structural changes in the corresponding electrodes before and after cycling.

The effects of oxygen vacancies on the Li-ion adsorption ability and electronic structure of  $(\text{Ni},\text{Co},\text{Mn})\text{Fe}_2\text{O}_{4-x}$  were analyzed using DFT calculations. The atomic structural models of  $(\text{Ni},\text{Co},\text{Mn})\text{Fe}_2\text{O}_4$  and  $(\text{Ni},\text{Co},\text{Mn})\text{Fe}_2\text{O}_{4-x}$  were constructed and are displayed in Figure 7a,b, respectively. The adsorption energy of oxygen vacancy-rich  $(\text{Ni},\text{Co},\text{Mn})\text{Fe}_2\text{O}_{4-x}$  was  $-2.09 \text{ eV}$ , which was lower than that of pristine  $(\text{Ni},\text{Co},\text{Mn})\text{Fe}_2\text{O}_4$  ( $-1.89 \text{ eV}$ ; Figure 7c), supporting that the introduction of oxygen vacancies can promote the adsorption and diffusion toward lithium as well as provide more active sites at the same time. Figure 7d and e show the projected density of state (PDOS) of pristine  $(\text{Ni},\text{Co},\text{Mn})\text{Fe}_2\text{O}_4$  and oxygen vacancy-rich  $(\text{Ni},\text{Co},\text{Mn})\text{Fe}_2\text{O}_{4-x}$ . Neither of them have a bandgap, suggesting their band-conducting feature. Meanwhile, in the PDOSs of  $(\text{Ni},\text{Co},\text{Mn})\text{Fe}_2\text{O}_4$  and  $(\text{Ni},\text{Co},\text{Mn})\text{Fe}_2\text{O}_{4-x}$ , the energy 0 point was chosen as the Fermi energy level. Around the Fermi levels, the PDOS of  $(\text{Ni},\text{Co},\text{Mn})\text{Fe}_2\text{O}_{4-x}$  appears more dense than that of  $(\text{Ni},\text{Co},\text{Mn})\text{Fe}_2\text{O}_4$ , which confirms that oxygen vacancies can modulate the electronic structure and may further promote  $\text{Li}^+$  storage [34]. According to the above analysis, it was revealed that the oxygen defects on the  $(\text{NiCoMn})\text{Fe}_2\text{O}_4$  surface can provide outstanding Li capture capacity, leading to excellent electrochemical properties and lifetime.

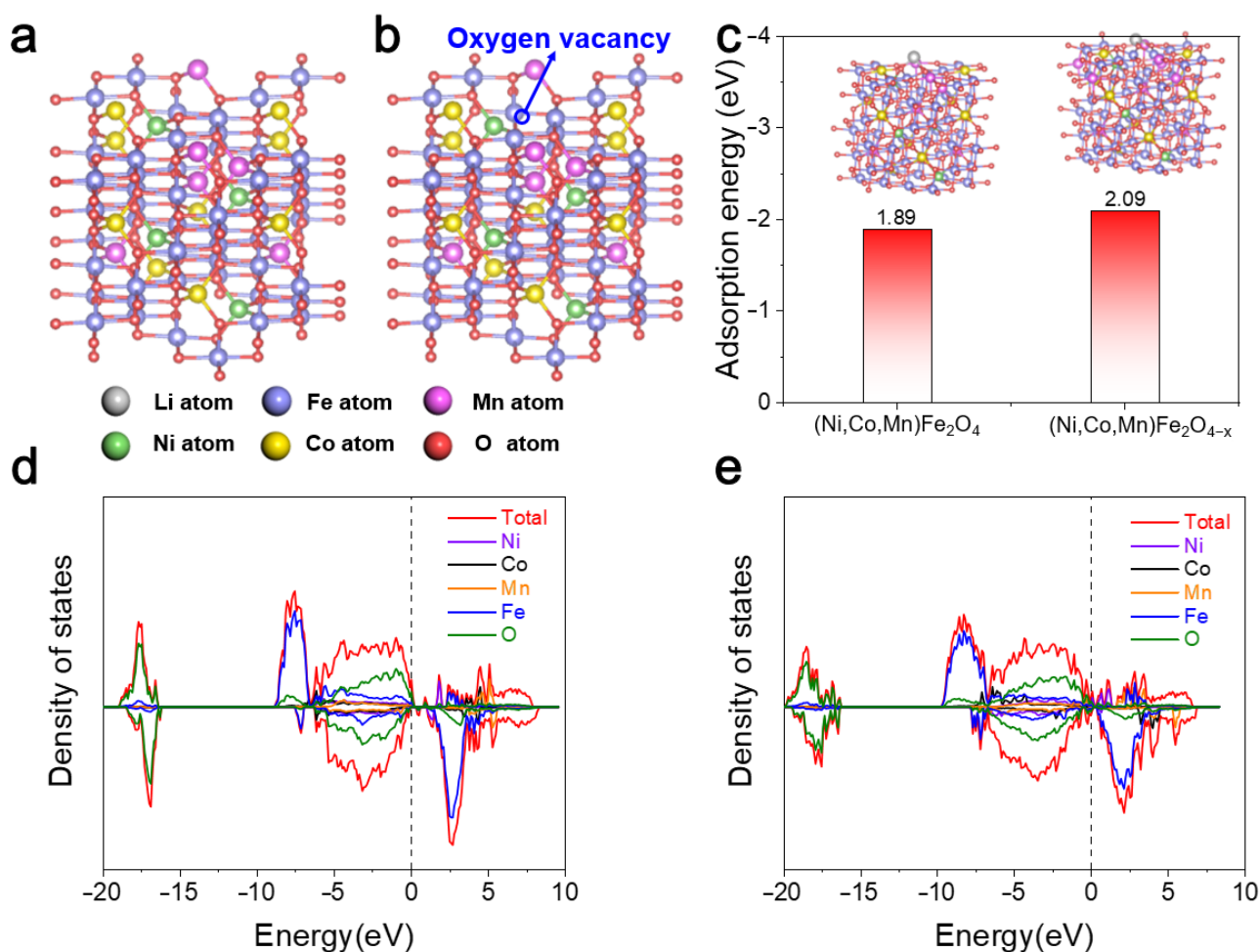


**Figure 7.** Crystal structures of (a)  $(\text{Ni,Co,Mn})\text{Fe}_2\text{O}_4$  and (b)  $(\text{Ni,Co,Mn})\text{Fe}_2\text{O}_{4-x}$ . (c) Calculated adsorption energy of Li on the surface of  $(\text{Ni,Co,Mn})\text{Fe}_2\text{O}_4$  and  $(\text{Ni,Co,Mn})\text{Fe}_2\text{O}_{4-x}$  (insert: optimized Li adsorption configuration). Density of states of (d)  $(\text{Ni,Co,Mn})\text{Fe}_2\text{O}_4$  and (e)  $(\text{Ni,Co,Mn})\text{Fe}_2\text{O}_{4-x}$ .

Table S1 shows a comparison of the electrochemical properties of as-obtained  $(\text{Ni,Co,Mn})\text{Fe}_2\text{O}_{4-x}$  and previously reported materials. It can be found from the table that the lithium storage performance of the  $(\text{Ni,Co,Mn})\text{Fe}_2\text{O}_{4-x}$  material is higher than that of many reported spinel-structured oxides and multi-component metal oxides. It seems that high-entropy oxides with five cations present lower electrochemical properties than  $(\text{Ni,Co,Mn})\text{Fe}_2\text{O}_{4-x}$ . In fact, regardless of high-entropy oxides with five cations or the material designed in this paper, electrochemical properties are determined by the composition and crystal structure of materials, as well as the size, specific surface area, three-dimensional structure and other factors. To develop high-performance anode materials, the above aspects need to be carefully designed and balanced. Good Li storage properties could be ascribed to three aspects. Firstly, the lithiation/delithiation process of multi-component transition metal oxides is carried out stepwise (wide CV peak), which is related to the entropy stabilization effect and the multi-cation synergistic effect [19–22,38]. This greatly inhibits the expansion and cracking of active materials (Figure 6) caused by short time and drastic volume changes in monometallic oxides and improves the electrochemical stability of materials in long cycling. Secondly, a large number of oxygen vacancies provide abundant active sites, improve the adsorption capacity of oxides towards lithium, improve the electronic structure of the material and thus enhance the cyclic stability and rate performance of the material. Thirdly, spinel oxides possess the advantages of narrow band gap and higher electroconductibility than traditional oxides, which are beneficial to improving the rate performance of materials. This paper provides a strategy

for the preparation of spinel-structured, multi-component transition metal oxides with abundant oxygen vacancies, which can have positive effects on the composition design and development of related materials and the improvement of the properties of novel anode materials for LIB applications.

#### 4. Conclusions

In summary, a spinel-type, multi-component transition metal oxide,  $(\text{Ni,Co,Mn})\text{Fe}_2\text{O}_{4-x}$ , with oxygen vacancies was designed and prepared using a melt-spinning and dealloying strategy. When utilized as anode material for LIBs, the  $(\text{Ni,Co,Mn})\text{Fe}_2\text{O}_{4-x}$  material presented good electrochemical properties, delivering a reversible capacity of  $1240.2 \text{ mAh g}^{-1}$  at  $100 \text{ mA g}^{-1}$  for 200 cycles and then at  $300 \text{ mA g}^{-1}$  for 300 cycles. It also presented extremely long cycle stability, revealing a reversible capacity of  $650.5 \text{ mAh g}^{-1}$  at  $2 \text{ A g}^{-1}$  for 1200 cycles. Our DFT calculations revealed the pivotal role of oxygen defects in the ion transport process and in adjusting the electronic structure, leading to improved Li capture ability. Moreover, the electrode material uncovered a spectacular structural reservation capacity after cycling because of the entropy stabilization effect and the multi-cation synergistic effect, which is a vital stimulus for satisfactory cycle stability. This work presents positive results for the composition design and development of novel, spinel-structured, multi-component transition metal oxides with abundant oxygen vacancies. The as-fabricated materials are aimed to be applied as alternative LIB anode materials.

**Supplementary Materials:** The following supporting information can be downloaded at: <https://www.mdpi.com/article/10.3390/batteries9010054/s1>, S1: Experiments and Computation, Figure S1: SEM images and size statistics of products, Figure S2: EPR analysis and crystal structure model, Figure S3: EDS analysis, Figure S4: XRD of precursors and corresponding dealloyed products, Figure S5: CV curves of  $\text{Fe}_3\text{O}_4$  and  $\text{Fe}_3\text{O}_4/\text{Mn}_3\text{O}_4$ , Figure S6: Charge/discharge profiles of experimental materials, Table S1: Comparison of lithium storage properties, Table S2: List of Li-ion diffusion coefficients of experimental materials [34,38,42–45,55].

**Author Contributions:** Conceptualization, Y.L., C.Q. and Z.W. (Zhifeng Wang); methodology, Y.L., W.Z. and Z.W. (Zhifeng Wang); investigation, L.D., Z.W. (Zigang Wang), C.J. and F.D.; data curation, L.D., C.J. and F.D.; writing—original draft preparation, L.D. and Z.W. (Zigang Wang); writing—review and editing, Y.L., W.Z. and Z.W. (Zhifeng Wang); visualization, Z.W. (Zigang Wang) and C.Q.; supervision, Y.L., W.Z. and C.Q.; project administration, Z.W. (Zhifeng Wang); funding acquisition, Y.L. and Z.W. (Zhifeng Wang). All authors have read and agreed to the published version of the manuscript.

**Funding:** The authors would like to acknowledge the financial support from Natural Science Foundation of Hebei Province, China (E2020202071), Hebei Higher Education Teaching Reform Research and Practice Project, China (2021GJJG050), and Science and Technology Project of Hebei Education Department, China (ZD2020177).

**Informed Consent Statement:** Not applicable.

**Data Availability Statement:** The data presented in this study are available upon request from the corresponding author.

**Acknowledgments:** The numerical calculations in this paper were performed using TianHe-2 at LvLiang Cloud Computing Center of China. C.J. and F.D. acknowledge the support from Innovative Top-Notch Student Training Program and Innovation and Entrepreneurship Training Program (202210080001) of Hebei University of Technology.

**Conflicts of Interest:** The authors declare no conflict of interest.

#### References

1. Gao, S.S.; Wei, T.R.; Sun, J.Q.; Liu, Q.; Ma, D.; Liu, W.X.; Zhang, S.S.; Luo, J.; Liu, X.J. Atomically dispersed metal-based catalysts for Zn–CO<sub>2</sub> batteries. *Small Struct.* **2022**, *3*, 2200086. [CrossRef]
2. Salian, A.; Mandal, S. Entropy stabilized multicomponent oxides with diverse functionality—A review. *Crit. Rev. Solid State Mat. Sci.* **2021**, *47*, 142–193. [CrossRef]

3. Tomboc, G.M.; Zhang, X.; Choi, S.; Kim, D.; Lee, L.Y.S.; Lee, K. Stabilization, characterization, and electrochemical applications of high-entropy oxides: Critical assessment of crystal phase–properties relationship. *Adv. Funct. Mater.* **2022**, *32*, 2205142. [[CrossRef](#)]
4. Chen, Z.; Danilov, D.L.; Eichel, R.A.; Notten, P.H.L. Porous electrode modeling and its applications to Li-ion batteries. *Adv. Energy Mater.* **2022**, *12*, 202201506. [[CrossRef](#)]
5. Poizot, P.; Laruelle, S.; Grugeon, S.; Dupont, L.; Tarascon, J.M. Nano-sized transition-metal oxides as negative-electrode materials for lithium-ion batteries. *Nature* **2000**, *407*, 496–499. [[CrossRef](#)]
6. Choi, Y.S.; Choi, W.; Yoon, W.S.; Kim, J.M. Unveiling the genesis and effectiveness of negative fading in nanostructured iron oxide anode materials for lithium-ion batteries. *ACS Nano* **2022**, *16*, 631–642. [[CrossRef](#)]
7. Roy, K.; Banerjee, A.; Ogale, S. Search for new anode materials for high performance Li-ion batteries. *ACS Appl. Mater. Interfaces* **2022**, *14*, 20326–20348. [[CrossRef](#)]
8. Sharma, A.; Rajkamal, A.; Kobi, S.; Kumar, B.S.; Paidi, A.K.; Chatterjee, A.; Mukhopadhyay, A. Addressing the high-voltage structural and electrochemical instability of Ni-containing layered transition metal (TM) oxide cathodes by “Blocking” the “TM-migration” pathway in the Lattice. *ACS Appl. Mater. Interfaces* **2021**, *13*, 25836–25849. [[CrossRef](#)]
9. Shen, Y.; Jiang, Y.; Yang, Z.; Dong, J.; Yang, W.; An, Q.; Mai, L. Electronic structure modulation in MoO<sub>2</sub>/MoP heterostructure to induce fast electronic/ionic diffusion kinetics for lithium storage. *Adv. Sci.* **2022**, *9*, e2104504. [[CrossRef](#)]
10. Lin, J.; Zeng, C.; Lin, X.; Xu, C.; Xu, X.; Luo, Y. Metal-organic framework-derived hierarchical MnO/Co with oxygen vacancies toward elevated-temperature Li-ion Battery. *ACS Nano* **2021**, *15*, 4594–4607. [[CrossRef](#)]
11. Aghamohammadi, H.; Eslami-Farsani, R. Synthesis and electrochemical performance of TiNb<sub>2</sub>O<sub>7</sub> nanoparticles grown on electrochemically prepared graphene as anode materials for Li-ion batteries. *J. Power Sources* **2022**, *535*, 231418. [[CrossRef](#)]
12. Liang, J.; Deng, W.; Zhou, X.; Liang, S.; Hu, Z.; He, B.; Shao, G.; Liu, Z. High Li-ion conductivity artificial interface enabled by Li-grafted graphene oxide for stable Li metal pouch cell. *ACS Appl. Mater. Interfaces* **2021**, *13*, 29500–29510. [[CrossRef](#)] [[PubMed](#)]
13. Deng, Q.; Wang, M.; Peng, Z.; Liu, Z.; Fan, H.; Zhang, Y. Ultrafast Li<sup>(+)</sup> diffusion kinetics enhanced by cross-stacked nanosheets loaded with Co<sub>3</sub>O<sub>4</sub>@NiO nanoparticles: Constructing superstructure to enhance Li-ion half/full batteries. *J. Colloid Interface Sci.* **2021**, *585*, 51–60. [[CrossRef](#)] [[PubMed](#)]
14. Darbar, D.; Anilkumar, M.R.; Rajagopalan, V.; Bhattacharya, I.; Elim, H.I.; Ramakrishnappa, T.; Ezema, F.I.; Jose, R.; Reddy, M.V. Studies on spinel cobaltites, MCo<sub>2</sub>O<sub>4</sub> (M = Mn, Zn, Fe, Ni and Co) and their functional properties. *Ceram. Int.* **2018**, *44*, 4630–4639. [[CrossRef](#)]
15. Reddy, M.V.; Yao Quan, C.; Adams, S. Mg, Cu, Zn doped Fe<sub>2</sub>O<sub>3</sub> as an electrode material for Li-ion batteries. *Mater. Lett.* **2018**, *212*, 186–192. [[CrossRef](#)]
16. Barqi, J.; Masoudpanah, S.M.; Hasheminasari, M.; Liu, X. Nanoribbon-like NiCo<sub>2</sub>O<sub>4</sub>/reduced graphene oxide nanocomposite for high-performance hybrid supercapacitor. *J. Alloys Compd.* **2022**, *930*, 167509. [[CrossRef](#)]
17. Li, T.; Li, X.; Wang, Z.; Guo, H.; Li, Y. A novel NiCo<sub>2</sub>O<sub>4</sub> anode morphology for lithium-ion batteries. *J. Mater. Chem. A* **2015**, *3*, 11970–11975. [[CrossRef](#)]
18. Reddy, M.V.; Xu, Y.; Rajarajan, V.; Ouyang, T.; Chowdari, B.V.R. Template free facile molten synthesis and energy storage studies on MCo<sub>2</sub>O<sub>4</sub> (M = Mg, Mn) as anode for Li-ion batteries. *ACS Sustain. Chem. Eng.* **2015**, *3*, 3035–3042. [[CrossRef](#)]
19. Grzesik, Z.; Smoła, G.; Miszczak, M.; Stygar, M.; Dąbrowa, J.; Zajusz, M.; Świerczek, K.; Danielewski, M. Defect structure and transport properties of (Co,Cr,Fe,Mn,Ni)<sub>3</sub>O<sub>4</sub> spinel-structured high entropy oxide. *J. Eur. Ceram. Soc.* **2020**, *40*, 835–839. [[CrossRef](#)]
20. Zhao, J.; Yang, X.; Huang, Y.; Du, F.; Zeng, Y. Entropy stabilization effect and oxygen vacancies enabling spinel oxide highly reversible lithium-ion storage. *ACS Appl. Mater. Interfaces* **2021**, *13*, 58674–58681. [[CrossRef](#)]
21. Dąbrowa, J.; Stygar, M.; Mikula, A.; Knapik, A.; Mroczka, K.; Tejchman, W.; Danielewski, M.; Martin, M. Synthesis and microstructure of the (Co,Cr,Fe,Mn,Ni)<sub>3</sub>O<sub>4</sub> high entropy oxide characterized by spinel structure. *Mater. Lett.* **2018**, *216*, 32–36. [[CrossRef](#)]
22. Huang, C.Y.; Huang, C.W.; Wu, M.C.; Patra, J.; Xuyen Nguyen, T.; Chang, M.T.; Clemens, O.; Ting, J.M.; Li, J.; Chang, J.K. Atomic-scale investigation of lithiation/delithiation mechanism in high-entropy spinel oxide with superior electrochemical performance. *Chem. Eng. J.* **2021**, *420*, 129838. [[CrossRef](#)]
23. Nguyen, T.X.; Tsai, C.C.; Patra, J.; Clemens, O.; Chang, J.K.; Ting, J.M. Co-free high entropy spinel oxide anode with controlled morphology and crystallinity for outstanding charge/discharge performance in lithium-ion batteries. *Chem. Eng. J.* **2022**, *430*, 132658. [[CrossRef](#)]
24. Patra, J.; Nguyen, T.X.; Tsai, C.C.; Clemens, O.; Li, J.; Pal, P.; Chan, W.K.; Lee, C.H.; Chen, H.Y.T.; Ting, J.M.; et al. Effects of elemental modulation on phase purity and electrochemical properties of Co-free high-entropy spinel oxide anodes for lithium-ion batteries. *Adv. Funct. Mater.* **2022**, *32*, 2110992. [[CrossRef](#)]
25. Mohamed, H.S.H.; Li, C.F.; Wu, L.; Shi, W.H.; Dong, W.D.; Liu, J.; Hu, Z.Y.; Chen, L.H.; Li, Y.; Su, B.L. Growing ordered CuO nanorods on 2D Cu/g-C<sub>3</sub>N<sub>4</sub> nanosheets as stable freestanding anode for outstanding lithium storage. *Chem. Eng. J.* **2021**, *407*, 126941. [[CrossRef](#)]
26. Han, Y.; Sang, Z.; Liu, D.; Zhang, T.; Feng, J.; Si, W.; Dou, S.X.; Liang, J.; Hou, F. Lithiophilic and conductive V<sub>2</sub>O<sub>3</sub>/VN nanosheets as regulating layer for high-rate, high-areal capacity and dendrite-free lithium metal anodes. *Chem. Eng. J.* **2021**, *420*, 129787. [[CrossRef](#)]

27. Alli, U.; McCarthy, K.; Baragau, I.A.; Power, N.P.; Morgan, D.J.; Dunn, S.; Killian, S.; Kennedy, T.; Kellici, S. In-situ continuous hydrothermal synthesis of TiO<sub>2</sub> nanoparticles on conductive N-doped MXene nanosheets for binder-free Li-ion battery anodes. *Chem. Eng. J.* **2022**, *430*, 132976. [[CrossRef](#)]
28. Zhang, W.; Jin, H.; Chen, G.; Zhang, J. Hierarchical 3D N-CNT/Sb<sub>2</sub>MoO<sub>6</sub> for dendrite-free lithium metal battery. *Chem. Eng. J.* **2021**, *420*, 129614. [[CrossRef](#)]
29. Yan, Z.C.; Chen, Q.; Zhang, H.; Kim, K.B.; Wang, W.M. The effects of Al<sub>2</sub>Au phase and oxide film on dealloying performances of Al<sub>50</sub>Au<sub>50</sub> ribbon. *Intermetallics* **2022**, *147*, 107611. [[CrossRef](#)]
30. Xia, Q.; He, S.Y.; Zhang, W.; Xiang, Q.C.; Qu, Y.D.; Ren, Y.L.; Qiu, K.Q. Degradation efficiency of Mg<sub>65</sub>Cu<sub>25-x</sub>Ag<sub>x</sub>Y<sub>10</sub> nanoporous dealloyed ribbons on pesticide wastewater. *Trans. Nonferrous Met. Soc. China* **2022**, *32*, 1472–1484. [[CrossRef](#)]
31. Luo, C.; Wang, Z.G.; Chen, Y.X.; Zhao, Y.M.; Han, Q.Q.; Qin, C.L.; Wang, Z.F. Eutectic-derived bimodal porous Ni@NiO nanowire networks for high-performance Li-ion battery anodes. *Int. J. Energy Res.* **2022**, *46*, 24654–24666. [[CrossRef](#)]
32. Tan, F.Q.; Yu, B.; Bai, Q.G.; Zhang, Z.H. Potentiostatic dealloying fabrication and electrochemical actuation performance of bulk nanoporous palladium. *Metals* **2022**, *12*, 2153. [[CrossRef](#)]
33. Lu, C.; Wang, J.; Cao, D.; Guo, F.; Hao, X.; Li, D.; Shi, W. Synthesis of magnetically recyclable g-C<sub>3</sub>N<sub>4</sub>/NiFe<sub>2</sub>O<sub>4</sub> S-scheme heterojunction photocatalyst with promoted visible-light-response photo-Fenton degradation of tetracycline. *Mater. Res. Bull.* **2023**, *158*, 112064. [[CrossRef](#)]
34. Du, W.; Zheng, Y.; Liu, X.; Cheng, J.; Reddy, R.C.K.; Zeb, A.; Lin, X.; Luo, Y. Oxygen-enriched vacancy spinel MFe<sub>2</sub>O<sub>4</sub>/carbon (M = Ni, Mn, Co) derived from metal-organic frameworks toward boosting lithium storage. *Chem. Eng. J.* **2023**, *451*, 138626. [[CrossRef](#)]
35. Liu, X.; Xing, Y.; Xu, K.; Zhang, H.; Gong, M.; Jia, Q.; Zhang, S.; Lei, W. Kinetically accelerated lithium storage in high-entropy (LiMgCoNiCuZn)O enabled by oxygen vacancies. *Small* **2022**, *18*, e2200524. [[CrossRef](#)] [[PubMed](#)]
36. Viet Thieu, Q.Q.; Kidanu, W.G.; Nguyen, H.D.; Thi Nguyen, T.L.; Phung Le, M.L.; Nguyen, V.H.; Nguyen, D.Q.; Tran, N.T.; Nguyen, X.V.; Kim, I.T.; et al. Spinel Ni-ferrite advanced high-capacity anode for Li-ion batteries prepared via coprecipitation route. *Ceram. Int.* **2022**, *48*, 31470–31477. [[CrossRef](#)]
37. Wang, D.; Jiang, S.; Duan, C.; Mao, J.; Dong, Y.; Dong, K.; Wang, Z.; Luo, S.; Liu, Y.; Qi, X. Spinel-structured high entropy oxide (FeCoNiCrMn)<sub>3</sub>O<sub>4</sub> as anode towards superior lithium storage performance. *J. Alloys Compd.* **2020**, *844*, 156158. [[CrossRef](#)]
38. Xiao, B.; Wu, G.; Wang, T.; Wei, Z.; Sui, Y.; Shen, B.; Qi, J.; Wei, F.; Zheng, J. High-entropy oxides as advanced anode materials for long-life lithium-ion Batteries. *Nano Energy* **2022**, *95*, 106962. [[CrossRef](#)]
39. Nguyen, T.X.; Patra, J.; Chang, J.-K.; Ting, J.-M. High entropy spinel oxide nanoparticles for superior lithiation–delithiation performance. *J. Mater. Chem. A* **2020**, *8*, 18963–18973. [[CrossRef](#)]
40. Sun, Z.; Zhao, Y.; Sun, C.; Ni, Q.; Wang, C.; Jin, H. High entropy spinel-structure oxide for electrochemical application. *Chem. Eng. J.* **2022**, *431*, 133448. [[CrossRef](#)]
41. Luo, X.F.; Patra, J.; Chuang, W.T.; Nguyen, T.X.; Ting, J.M.; Li, J.; Pao, C.W.; Chang, J.K. Charge-discharge mechanism of high-entropy Co-free spinel oxide toward Li<sup>+</sup> storage examined using operando quick-scanning X-ray absorption spectroscopy. *Adv. Sci.* **2022**, *9*, e2201219. [[CrossRef](#)]
42. Ghosh, S.; de Donder, T.; Gunnarsson, K.; Kumar, V.K.; Martha, S.K.; Svedlindh, P.; Kessler, V.G.; Seisenbaeva, G.A.; Pol, V.G. Investigating the stable operating voltage for the MnFe<sub>2</sub>O<sub>4</sub> Li-ion battery anode. *Sustain. Energy Fuels* **2021**, *5*, 1904–1913. [[CrossRef](#)]
43. Zhu, L.; Han, T.; Ding, Y.; Long, J.; Lin, X.; Liu, J. A metal-organic-framework derived NiFe<sub>2</sub>O<sub>4</sub>@NiCo-LDH nanocube as high-performance lithium-ion battery anode under different temperatures. *Appl. Surf. Sci.* **2022**, *599*, 153953. [[CrossRef](#)]
44. Yang, C.; Peng, C.; Chen, P.; Ma, C.; Guo, K.; Cheng, Y. Insights into electrochemical performances of NiFe<sub>2</sub>O<sub>4</sub> for lithium-ion anode materials. *J. Alloys Compd.* **2022**, *896*, 163079. [[CrossRef](#)]
45. Tan, S.; Zhao, Q.; Geng, Y.; Yin, J.; Zhou, C.; Zhang, P.; Chu, X.; Xu, S.; Lu, M.; Wang, L.; et al. Enhanced lithium storage capacitance of layered CoFe<sub>2</sub>O<sub>4</sub>&V<sub>2</sub>CT hybrid anode material synthesized by in-situ hydrothermal method. *J. Alloys Compd.* **2022**, *918*, 165778. [[CrossRef](#)]
46. Mozdierz, M.; Swierczek, K.; Dabrowa, J.; Gajewska, M.; Hanc, A.; Feng, Z.; Cieslak, J.; Kadziolka-Gawel, M.; Plotek, J.; Marzec, M.; et al. High-entropy Sn<sub>0.8</sub>(Co<sub>0.2</sub>Mg<sub>0.2</sub>Mn<sub>0.2</sub>Ni<sub>0.2</sub>Zn<sub>0.2</sub>)<sub>2.2</sub>O<sub>4</sub> conversion-alloying anode material for Li-ion cells: Altered lithium storage mechanism, activation of Mg, and origins of the improved cycling stability. *ACS Appl. Mater. Interfaces* **2022**, *14*, 42057–42070. [[CrossRef](#)] [[PubMed](#)]
47. Wang, Z.F.; Fei, P.Y.; Xiong, H.Q.; Qin, C.L.; Zhao, W.M.; Liu, X.Z. CoFe<sub>2</sub>O<sub>4</sub> nanoplates synthesized by dealloying method as high performance Li-ion battery anodes. *Electrochim. Acta* **2017**, *252*, 295–305. [[CrossRef](#)]
48. He, G.G.; Wen, Y.; Ma, C.; Li, X.Y.; Gao, L.M.; Sun, Z.B. Photocatalytic hydrogen evolution of nanoporous CoFe<sub>2</sub>O<sub>4</sub> and NiFe<sub>2</sub>O<sub>4</sub> for water splitting. *Int. J. Hydrog. Energy* **2021**, *46*, 5369–5377. [[CrossRef](#)]
49. Xie, T.; Zhang, Z.Y.; Zheng, H.Y.; Xu, K.D.; Hu, Z.; Lei, Y. Enhanced photothermal catalytic performance of dry reforming of methane over Ni/mesoporous TiO<sub>2</sub> composite catalyst. *Chem. Eng. J.* **2022**, *429*, 132507. [[CrossRef](#)]
50. Yao, L.H.; Zhao, J.G.; Pan, Q.L.; Li, X.Y.; Xing, B.Y.; Jiang, S.; Song, J.; Pang, M.J. Tailoring NiO@NiFe<sub>2</sub>O<sub>4</sub>/CNTs triphase hybrids towards high-performance anode for lithium-ion batteries. *J. Alloys Compd.* **2022**, *912*, 165209. [[CrossRef](#)]
51. Li, R.R.; Long, Z.W.; Wu, C.Q.; Dai, H.; Li, W.; Bai, L.; Qiao, H.; Wang, K.L. Metal-organic frameworks-derived porous NiCo<sub>2</sub>O<sub>4</sub>/carbon composite nanofibers as anodes for Li/Na-ion batteries. *J. Alloys Compd.* **2023**, *936*, 168359. [[CrossRef](#)]

52. Yang, X.; Huang, Y.N.; Wang, M.J.; Miao, Z.R.; Liu, H.Z.; Chen, Z.M.; Yang, Z.Y.; Yu, J. Double hollow  $Zn_2SnO_4/SnO_2@N$ -doped carbon nanocubes as anode material for high-performance Li-ion batteries. *Chem. Phys. Lett.* **2023**, *813*, 140285. [[CrossRef](#)]
53. Keppeler, M.; Srinivasan, M. Interfacial phenomena/capacities beyond conversion reaction occurring in nano-sized transition-metal-oxide-based negative electrodes in lithium-ion batteries: A Review. *ChemElectroChem* **2017**, *4*, 2727–2754. [[CrossRef](#)]
54. Liu, Y.; Peng, W.; Zhang, J.; Li, S.; Hu, R.; Yuan, B.; Chen, G. Tuning the electronic properties of NiO anode by in-situ introducing metallic Cu for high capacity and long life-span lithium-ion batteries. *J. Alloys Compd.* **2022**, *918*, 165693. [[CrossRef](#)]
55. Chen, H.; Qiu, N.; Wu, B.; Yang, Z.; Sun, S.; Wang, Y. A new spinel high-entropy oxide  $(Mg_{0.2}Ti_{0.2}Zn_{0.2}Cu_{0.2}Fe_{0.2})_3O_4$  with fast reaction kinetics and excellent stability as an anode material for lithium ion batteries. *RSC Adv.* **2020**, *10*, 9736–9744. [[CrossRef](#)]

**Disclaimer/Publisher's Note:** The statements, opinions and data contained in all publications are solely those of the individual author(s) and contributor(s) and not of MDPI and/or the editor(s). MDPI and/or the editor(s) disclaim responsibility for any injury to people or property resulting from any ideas, methods, instructions or products referred to in the content.